Structure of dense plumes from a finite-height cylinder in laminar crossflow

Anna K. Pauls
University of Colorado Boulder
Lars T. Larson
University of Colorado Boulder
Aaron C. True
University of Colorado Boulder
John P. Crimaldi (john.crimaldi@colorado.edu)
University of Colorado Boulder

Short Report

Keywords: plumes in crossflow, dense plumes, active scalars, horseshoe vortex, finite-height-cylinder wakes

Posted Date: November 24th, 2023

DOI: https://doi.org/10.21203/rs.3.rs-3645146/v1

Additional Declarations: No competing interests reported.

Structure of dense plumes from a finite-height cylinder in laminar crossflow

Anna K. Pauls[1], Lars T. Larson[1], Aaron C. True[1] and John P. Crimaldi[1]

[1]Civil, Environmental, and Architectural Engineering, University of Colorado Boulder, 428 UCB, Boulder, CO, 80309, USA.

Contributing authors: anna.pauls@colorado.edu; lars.larson@colorado.edu; aaron.true@colorado.edu; john.crimaldi@colorado.edu;

Abstract

The Training Aid Delivery Device (TADD) is a cylindrical vessel designed to securely store hazardous substances while permitting their odors, which may be active or passive scalar quantities, to permeate the surrounding air; the device is commonly used for canine odor detection training. However, the structures of scalar plumes emanating from the cylinder are unknown, particularly with variations in ambient flow speed and odor properties. In this study, we performed numerical simulations of flow and scalar fields around the cylinder, for three laminar crossflow velocities and three odor densities. The flow field around the cylinder is characterized by a near-bed horseshoe vortex and a downwash-driven arch vortex formed in the wake. These vortices confine most of the odor downstream of the cylinder resulting in a persistent bimodal plume structure with symmetrical concentration peaks off of the centerline. Experimental concentration profiles measured with a photoionization detector (PID) in a low-speed wind tunnel confirmed the steadiness and main structural features of the simulated plumes. Increasing crossflow velocity decreases the transverse width of the plume, while increasing odorant density yields local body forces that enhance the horseshoe vortex and modify the plume structure. These modifications include increased transverse spread and strengthened bimodal peaks of the plume. This study advances understanding of dense plume dispersal patterns in the wake of finite-height cylinders in laminar crossflow.

Keywords: plumes in crossflow, dense plumes, active scalars, horseshoe vortex, finite-height-cylinder wakes

1 Introduction

Canine scent detection and localization plays a critical supporting role in the military, law enforcement, search and rescue, and other public health and safety operations. The use of canines in odor detection is often the best available strategy [1], with sensitivity to certain explosive compounds in the parts-per-trillion range [2]. Engineered sensors have limited sensitivity compared to canines [3], and common, portable field instruments such as photoionization detectors (PIDs) cannot discern between chemical compounds [4]. Combined sensor arrays such as electronic noses [5, 6] and metal oxide (MOX) sensors may provide sufficient chemical differentiation, temporal resolution, and portability but sacrifice sensitivity and require specialized signal processing [7]. Ion mobility spectrometers (IMS) are sometimes deployed in control points such as airports and checkpoints, though they remain a complementary tool in tandem with canines [8].

Canines can be trained to detect hazardous materials by using operant conditioning to teach desired behaviors. This involves a reinforcer that is of high value to the canine, such as food or toy(s), being rewarded for the appropriately completing the correct behavior [9]. The Training Aid Delivery Device (TADD) [10] was developed to safely contain hazardous materials while allowing odors to permeate freely (Fig. 1). The TADD is a cylindrical glass jar with an odor-permeable membrane held by a protective grid that prevents contact with its contents. The cylinder has previously been used in a study testing the ability of canines to detect SARS-CoV-2 [11], but the spatiotemporal plume that emanates from the device has not been investigated scientifically.

The aim of this study is to characterize the dynamics of plumes emanating from the cylinder into laminar crossflow. We use experimental and numerical approaches to quantify the distribution of the odor, that can be a passive or active scalar depending on its density, near the cylinder. The plume distribution is computed numerically for three odorant specific gravities with two laminar crossflow velocities and one ambient condition with zero crossflow. Odorant specific gravities greater than one are considered active scalars because their density creates additional body forces that modify the flow. The cylinder is modeled as a bed-mounted, finite-height cylinder with a scalar diffusing into a laminar crossflow from the exposed end. Several canonical flow features can be expected to form in the wake of the cylinder, and the interaction of a scalar field with these features will shape the spatial evolution of the plume. Though the geometry of a finite-height cylinder is simple, the velocity

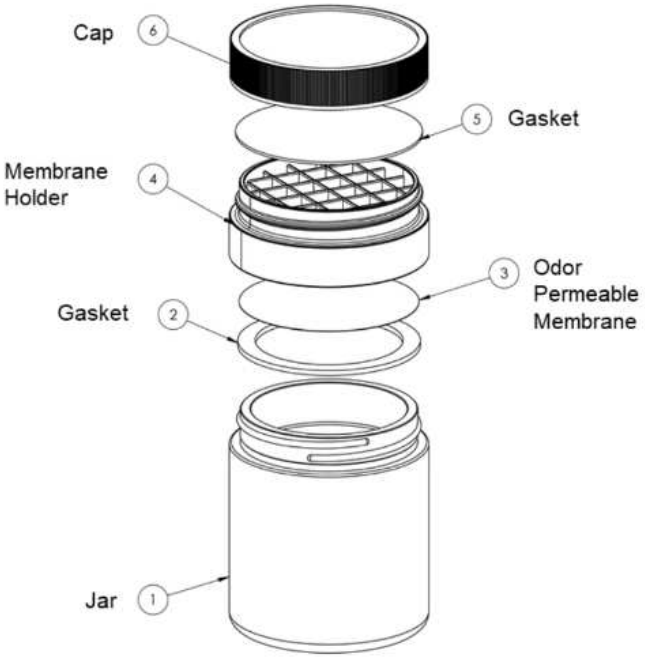

Fig. 1: Schematic of the Training Aid Delivery Device (TADD) [10].

field in crossflow is surprisingly complex. The dynamics of the wake are influenced by the Reynolds Number ($\mathrm{Re} = U\phi/\nu$), boundary layer thickness (δ), and aspect ratio ($\mathrm{AR} = h/\phi$) of the finite-height cylinder [12].

The onset of vortex shedding in the wake of the cylinder typically occurs with increasing Re but is suppressed by decreasing AR [13]. For an infinite-height cylinder with $\mathrm{Re} > 47$, counter-rotating vortices begin to periodically shed from the cylinder [14]. As Re continues to increase, the periodic shedding becomes antisymmetric, forming the von Karman vortex street [15]. However, the downwash created by flow over the free end of a finite-height cylinder suppresses vortex shedding when the AR of the obstacle is less than 6 [13, 16]. The impact of the downwash decreases as AR increases [13]. The presence of a recirculation region directly behind the cylinder is also depends on AR and Re. The region increases in size with increasing AR, but above a critical AR, the recirculation region size begins to decrease [13]. For fully turbulent Re and an AR between 1 and 2, the arch vortex will symmetrically shed off of the cylinder [13, 17].

For a cylinder with a small AR in steady laminar crossflow, a horseshoe vortex develops near the bed. Spanwise vortex tubes associated with the vorticity of the boundary layer wrap around the cylinder (Fig. 2), producing the characteristic shape of the horseshoe vortex [18, 19]. Additionally, finite-height cylinders in crossflow introduce vortex dynamics due to the downwash. For an $\mathrm{AR} < 3$, an arch vortex can form immediately behind the cylinder, created by

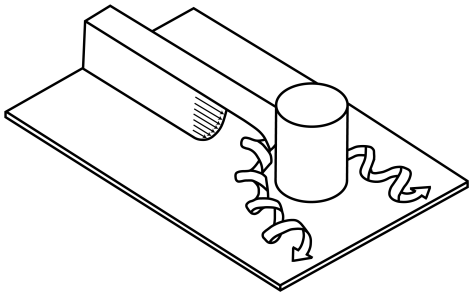

Fig. 2: Visual depiction of the horseshoe vortex formation adapted from [19].

vortex tubes surrounding the sides and top of the cylinder [20]. Additionally, tip vortices and trailing vortices may form near the trailing edge of the free end [12].

When scalars are introduced to the flow, their spatiotemporal distribution is driven by interactions with the vortex wake [21]. If the scalar is released on the centerline near the bed at a low height relative to the cylinder, it becomes entrained in the horseshoe vortex, following the divergent flow at the bed and the convergent flow on the top, resulting in a bimodal plume shape in the cylinder wake. This enhances the horizontal spread relative to vertical spread. Conversely, if the scalar is released at the same height as the free end of the cylinder, the scalar is carried over the free end of the cylinder and is brought downward to the bed. This creates a greater vertical spread as the rest of the scalar flows downstrean while interacting with the counter-rotating vortices from the horseshoe vortex [21].

Many studies of a scalar emanating from within a cylinder involve the dynamics of buoyant plumes at high Re as observed in smokestacks [16], chimneys [22], and hydrothermal vents [23]. Dense plumes are less frequently studied and typically relate to jet dispersion [24]. In the present study, we seek to expand current understanding of scalar flux from the free end of a cylinder in laminar crossflow by quantifying the impact of density and crossflow velocity on plume structure as it interacts with flow features in the cylinder wake.

2 Numerical Simulations

To investigate the spatiotemporal distribution of a plume emanating from the cylinder, we used a numerical model to vary crossflow and odorant density. The physics in the model was governed by the incompressible nondimensional Navier-Stokes (N-S) (Eq. 1), continuity (Eq. 2), and advection-difussion (A-D) equations (Eq. 3). The time scale and the length scale were nondimensionalized by the advective time scale (ϕ/U) and the diameter (ϕ), respectively, for all governing equations. Here, we denoted vector quantities in bold face, scalar

quantities in plain face, and nondimensional quantities with an asterisk.

$$\frac{\partial \mathbf{u}^*}{\partial t^*} + \mathbf{u}^* \cdot \nabla^* \mathbf{u}^* = \nabla^* p^* + \frac{1}{\mathrm{Re}} \nabla^{*2} \mathbf{u}^* + \mathrm{Ri} \tag{1}$$

$$\nabla^* \cdot \mathbf{u}^* = 0 \tag{2}$$

$$\frac{\partial C^*}{\partial t^*} + \mathbf{u}^* \cdot \nabla^* C^* = \frac{1}{\mathrm{Pe}} \nabla^{*2} C^* \tag{3}$$

The Richardson number (Eq. 4), appearing in Eq. 1 as Ri, locally compensated for the body forces that arose from the odorant density since explosive odors exhibit a spectrum of densities [25]. Ri is a function of specific gravity (SG) which is the ratio the of local odorant density relative to the density of air (ρ) (Eq. 5). Local density is a function of the local odor concentration multiplied by the difference in molecular weights (MW) of the odor and air. We used SG=SG($C_{\max}$) to define the different odorant density simulations.

$$\mathrm{Ri} = \frac{\phi g \mathrm{SG}}{U^2} \tag{4}$$

$$\mathrm{SG} = \frac{C(\mathrm{MW}_{\mathrm{scalar}} - \mathrm{MW}_{\mathrm{air}})}{\rho} + 1 \tag{5}$$

To find the maximum concentration ($C_{\max}$) of an odor (Eq. 6), the ideal gas law was used with saturation vapor pressure of the odor and lab temperature of approximately 298K. The Antoine equation provided a semi-empirical calculation of the vapor pressure, presuming Raoult's Law of Partial Pressures, which correlated the total pressure of the system with the vapor pressure of an odor and the mole fraction of that odor in the system. The application of Avogadro's Law determined the percentage of odor in the total mixture.

$$C_{\max} = \frac{P_{\mathrm{vap}}}{RT} \tag{6}$$

Given the dependence of SG on local odor concentration, the evolution of the scalar field dictated the evolution of the velocity field when SG > 1. When SG $= 1$, the odor was a passive scalar and A-D (Eq. 3) no longer influenced N-S (Eq. 1), but A-D (Eq. 3) remained coupled with N-S (1) through velocity. The Peclet Number (Pe) (Eq. 7), defined as the ratio of advection and molecular diffusion D to describe the mechanisms of mass transport in the system, appeared in Eq. 3.

$$\mathrm{Pe} = \frac{U\phi}{D} \tag{7}$$

The spatial domain of our model encompassed an 80 cm by 80 cm by 100 cm space (Fig. 3a). Both the inlet and outlet boundaries featured a cross-sectional area of 6400 cm^2. We defined the TADD as a finite-height cylinder with a diameter (ϕ) of 6.02 cm and a height (h) of 8.13 cm, resulting in an

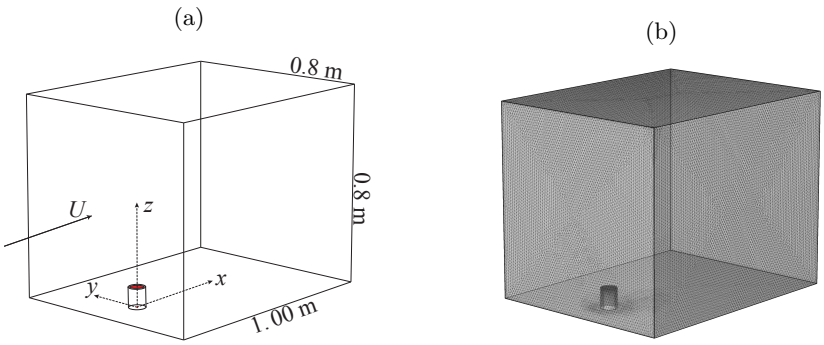

Fig. 3: (a) Numerical model domain. (b) Numerical model mesh.

AR of 1.35. We placed the center of the cylinder 18 cm downstream from the inlet, which served as the origin of the coordinate system.

The velocity field was initially defined by zero velocity and zero static pressure everywhere in the domain. For stability, we introduced the uniform inlet flow as a ramp function that transitioned to the desired velocity magnitude, U, within the first second of the simulation. We defined the outlet as a zero-static-pressure boundary condition with no back flow allowed. Suppressing back flow adjusted the outlet pressure to reduce the amount of fluid entering the domain through the boundary. The remaining sides of the domain and cylinder were no-slip boundary conditions to act as walls.

For the scalar field in the numerical model, initially there was no scalar present in the domain. Open boundary conditions in the scalar field were applied to the inlet and outlet boundary conditions in the velocity field. Where fluid flowed into the domain, an exterior scalar was prescribed as $C = 0$ on the open boundary. Where fluid flowed out of the domain, $\mathbf{n} \cdot (-D\nabla C) = 0$ was prescribed so no scalar can enter the domain. Impermeable scalar boundary conditions, defined as $-\mathbf{n}\cdot(-D\nabla C) = 0$, were assigned to the top, bottom, and sides of the domain, along with the walls of the extruded cylinder. On top of the cylinder, an impermeable boundary condition with a thickness of 3.3 mm was defined outside the red circle in Fig. 3a . This thickness represented the lip on the membrane holder (Fig. 1). The red circle corresponded to the mass flux condition applied to the model as $-\mathbf{n} \cdot (-D\nabla c + \mathbf{u}c) = q_z$. The mass flux rate was calculated using Eq. 8, and the mass flow rate was determined experimentally for acetone with a precision scale. Acetone was used in experiments later described. The mass flow rate for other explosive odors was calculated by scaling the acetone mass flow rate ($\dot{m}$) by the ratio of vapor pressures, defined by the Antoine equation, of the explosive odor and acetone.

We simulated the cases (Tab. 1) using the COMSOL MULTIPHYSICS package through a finite-element discretization scheme of N-S, continuity, and A-D equations. The mesh featured triangular and rectangular elements, with corner refinement reducing the element size near sharp edges and corners.

To assist with boundary layer production, the no-slip boundary conditions applied in the velocity field featured rectangular elements in the mesh. To test for convergence, mesh refinement was accomplished by increasing the degrees of freedom until further grid refinement yielded no discernable change in the solution. This process led to a final mesh with approximately 8.7×10^6 elements (Fig. 3b). The mesh had a minimum element size of 0.0008 m (0.013ϕ) and a maximum size of 0.0120 m (0.2ϕ).

$$q_z = \frac{\dot{m}}{\pi\phi^2/4} \tag{8}$$

The numerical integration scheme utilized an implicit second-order backward differentiation formula (BDF) with variable time steps. The step size was derived from a predetermined absolute and relative tolerance for the nonlinear solver. A direct PARDISO solver [26] handled the solution for the nonlinear system of equations.

Table 1: Table of computed cases.

Case No.	SG	Re	U (cm/s)	Pe
1	1.00	0	0	0
2	1.00	181	5.5	276
3	1.00	329	10.0	502
4	1.29	0	0	0
5	1.29	181	5.5	315
6	1.29	329	10.0	573
7	1.06	0	0	0
8	1.06	181	5.5	276
9	1.06	329	10.0	502

We performed numerical simulations for three velocities and three odorant SGs (Tab. 1). These cases provided insight into the dynamics of odor plumes emanating from a cylinder into laminar crossflow and further knowledge in dense plume dispersion.

We used the Q-criterion [27] to visualize vortical structures in the velocity produced by the numerical simulations. The Q-criterion was defined as $Q = \frac{1}{2}\left(\|\mathbf{\Omega}\|^2 - \|\mathbf{S}\|^2\right)$, where $\mathbf{S} = \frac{1}{2}(\frac{\partial u_i}{\partial x_j} + \frac{\partial u_j}{\partial x_i})$ is the strain rate tensor and $\mathbf{\Omega} = \frac{1}{2}(\frac{\partial u_i}{\partial x_j} - \frac{\partial u_j}{\partial x_i})$ is the rotation rate tensor. Positive values of Q occurred in regions where vorticity was dominant, whereas negative values occurred in strain-dominated regions [28]. For the remainder of the paper, we focus solely on a positive Q-criterion to determine vortical structures.

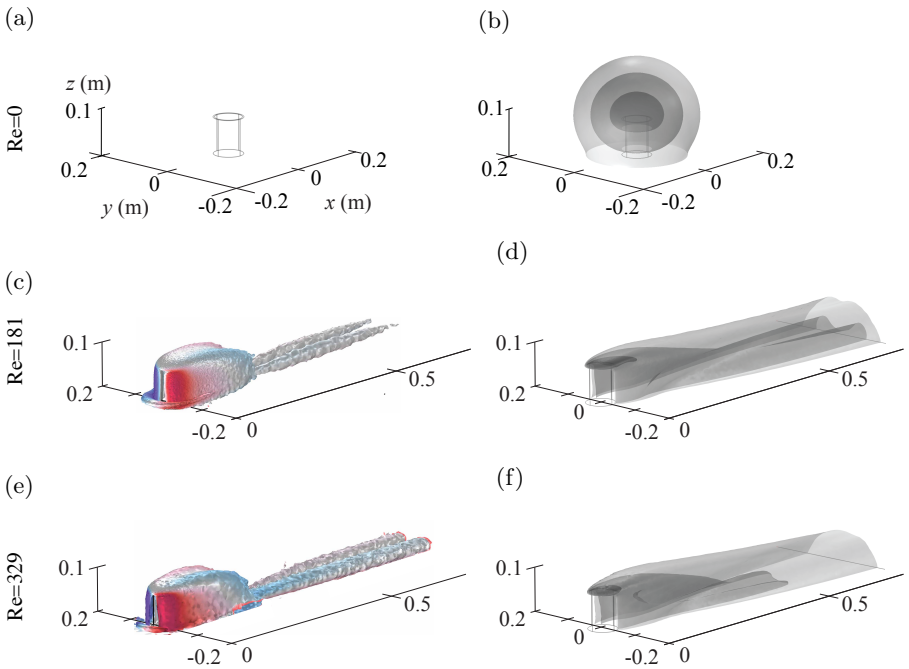

Fig. 4: Isosurface of a positive (vorticity-dominant) Q-criterion value (Q = 0.05 s^{-2}) is shown in the first column and odor isosurfaces (C^* = 0.01, 0.001, 0.0001) are shown in the second column for SG = 1 for Re = 0, 181, and 329. In the first column, the blue and red regions indicate negative and positive regions of transverse velocity, respectively. The Re = 0 solution are shown at t = 100 s while Re = 181 and Re = 329 is shown at steady state.

3 Numerical Results

3.1 Neutrally Buoyant Plume

We begin with simulation results for Cases 1-3 in Table 1 for neutrally buoyant plumes (SG = 1.00) emanating from the cylinder at three different Reynolds numbers (Fig. 4). For these cases, local odor concentrations do not influence the velocity field, but the structure of the velocity and associated vorticity fields directly impact the structure of the odor plumes. To emphasize the role of the vorticity field in shaping the plume, we present an isosurface of a vorticity-dominant Q-criterion (left column in Fig. 4) alongside isosurfaces of the associated scalar fields (right column in Fig. 4).

For Re = 0, there is no flow present, and the Q-criterion plot is blank (Fig. 4a). Spread of the odor from the cylinder in this case is driven purely by diffusion, resulting in odor isosurfaces that are approximately spherical in shape, except for where they are modified by the no-flux constraint at the bed (Fig. 4b). For Re = 0, the scalar field continues to develop indefinitely; the

odor isosurfaces shown in Fig. 4b correspond to a representative time of t = 100 s.

In the presence of crossflow, transverse vorticity in the upstream boundary layer flow is reoriented by the cylinder and wraps around it to form a horseshoe vortex in the cylinder wake. This vortex structure is clearly visible upstream in the in the Q-criterion isosurfaces in Figs. 4c (for Re = 181) and 4e (for Re = 329), particularly in the near-bed region upstream of the cylinder and in the centerline region of the far-field wake. The vortex structures are visibly stronger, and persist further downstream, for the higher-Re case. In these figures, red and blue hues superimposed on top of the Q-criterion isosurface indicate regions with negative and positive transverse velocities, respectively. Upstream flow farther from the bed passes over the cylinder and generates boundary layer vorticity on the top and sides of the cylinder. This vortical structure remains attached in the near-wake, forming an arch vortex. No vertical recirculation occurs in the near-wake due to downwash from the free end, consistent with previous studies of flows past low aspect ratio cylinders [16, 29]. The downwash from the top of the cylinder also suppresses periodic shedding due to low AR [13] such that the wake remains steady.

Odor isosurfaces for the two neutrally buoyant cases with crossflows are shown in Fig. 4d (for Re = 181) and Fig. 4f (for Re = 329). For these cases, the scalar field quickly reaches the steady state distribution shown in the figures. The odor leaves the free end of the cylinder and is entrained into the arch vortex, where downwash draws the odor to the bed in the near wake. Near the bed, the odor is captured by the horseshoe vortex, which dictates the general downstream shape of the plume. The plume narrows farther from the bed as the odor travels upwards with the rotation of the horseshoe vortex. On the centerline, the horseshoe vortex draws odor-free fluid down from above, creating a bimodal distribution. The plume plunges near the bed closer to the near wake of the cylinder as Re increases due to enhanced downwash and a thinner boundary layer over the free end of the cylinder (Fig. 4f).

3.2 Dense Plume

Next we consider simulation results for dense plumes (SG=1.29, Cases 4-6 in Table 1) emanating from the cylinder, again at three different Reynolds numbers (Fig. 5). For these cases, local odor concentrations increase the local fluid mixture density, actively altering the velocity field through coupling with the Ri term in Eq. 1.

For Re = 0, there is no crossflow, but the dense scalar field actively drives a flow that sinks from the top of the cylinder towards the bed, producing a vortex ring that is visible in the Q-criterion isosurface in Fig. 5a. Spread of the odor from away the cylinder in this case is driven largely by advection from the gravity current, which brings the odor to the bed and then radially outwards (Fig. 5b). The higher density of the mixture largely confines the plume to the near-bed region, while diffusion creates some vertical flux away from the bed. For this case, the velocity field and the scalar fields continue

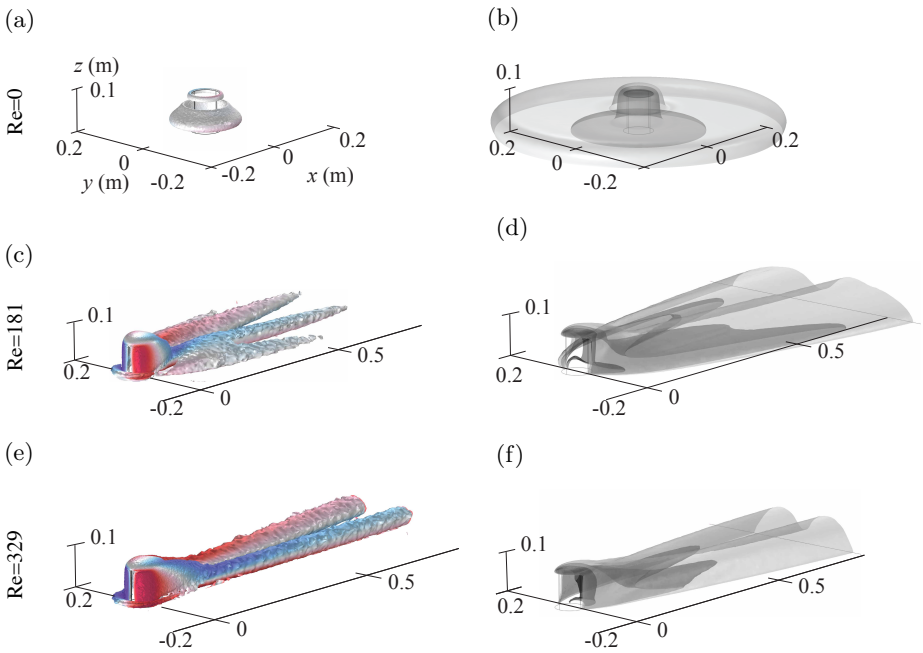

Fig. 5: Isosurface of a positive (vorticity-dominant) Q-criterion value (Q = 0.05 s^{-2}) is shown in the first column and odor isosurfaces (C^* = 0.01, 0.001, 0.0001) are shown in the second column for SG = 1.29 for Re = 0, 181, and 329. In the first column, the red and blue regions indicate negative and positive regions of transverse velocity, respectively. The Re = 0 solution is shown at t = 100 s while Re = 181 and Re = 329 are shown at steady state.

to develop indefinitely; the Q-criterion in Fig. 5a and the odor isosurfaces in Fig. 5b correspond to a representative time of t=100 s.

In the presence of a crossflow, the density of the odorant mixture suppresses the arch vortex and reinforces the horseshoe vortex. The local body forces accelerate the downwash, causing the arch vortex to collapse to the bed in the near wake. For Re = 181, two additional vortex tubes form downstream (Fig, 5c). These additional vortex tubes represent the deformation the horseshoe vortex goes under due to body force of the dense odor overcoming the vortex momentum (Fig. 6). Increasing Re also reinforces the horseshoe vortex and allows the arch vortex to extend further into the wake before collapsing (Fig. 5e).

The dense odor concentration distribution is characterized by three features: the odorant mixture is advected closer to the bed, the plume subsequently widens, and the bimodal distribution is enhanced (Fig. 5d). The increasing width of the plume is associated with the gravity current that diverges laterally in the horseshoe vortex near the bed. As before, the plume

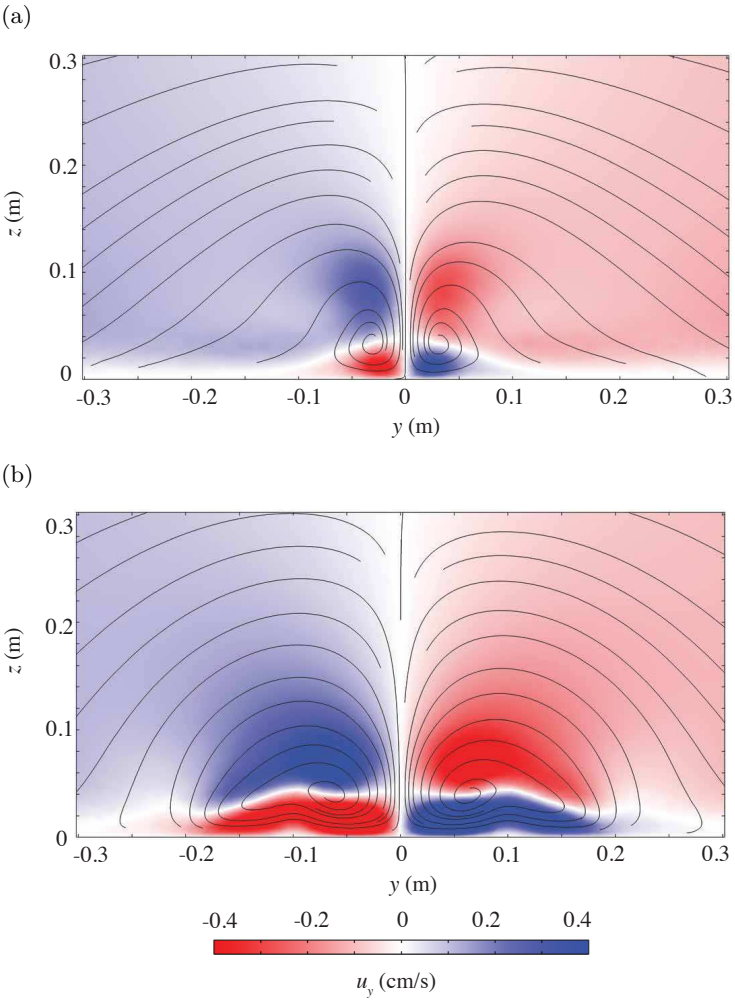

Fig. 6: Flow structure in the y-z plane in the far wake at $x = 0.4$ m. Streamlines show the position of the counter-rotating vortex cores, and transverse velocities are rendered in color. The top panel is $U = 5.5$ cm/s and SG=1.00 (Case 2). The bottom panel is $U = 5.5$ cm/s and SG=1.29 (Case 5).

narrows with increasing Re and the bimodality becomes more pronounced (Fig. 5f).

The two counter-rotating streamwise horseshoe vortices in the wake entrain fluid towards the bed along the centerline, and away from the centerline near the bed. These dynamics are illustrated in a y-z plane slice at $x = 0.4$ m for SG=1.00 (Case 2, Fig. 6a) and SG=1.29 (Case 5, Fig. 6b) where the streamlines illustrate the location of the vortex cores and associated fluid entrainment.

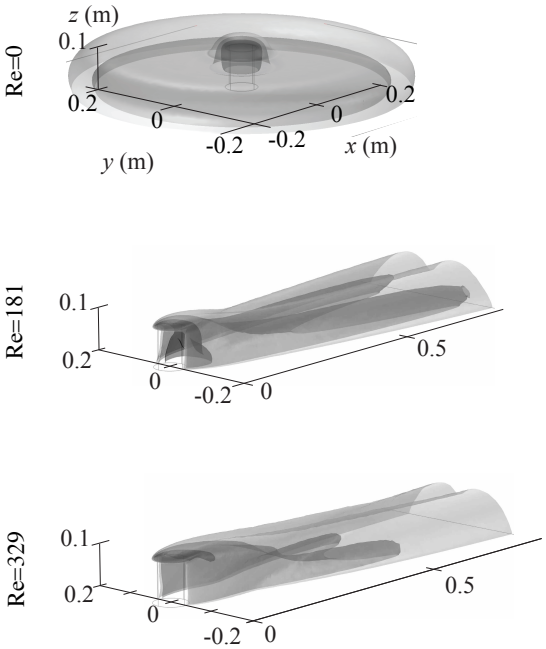

Fig. 7: Odor isosurfaces ($C^* = 0.01, 0.001, 0.0001$) for SG = 1.06 for Re = 0, 181, and 329. The Re = 0 solution is shown at t = 100 s while Re = 181 and Re = 329 are shown at steady state.

The dense odor case produces stronger transverse velocity due to the positive feedback mechanism between the scalar and velocity fields.

Cases 4-6 modeled above for SG =1.29 correspond to the density of saturated acetone vapor (SG = 1.29), chosen to match laboratory experiments in section 4, which use acetone vapor as the dense odor. Many explosives that might be used in the TADD for canine training would spread as neutrally buoyant plumes (subsection 3.1) because their vapor pressures are sufficiently low to constrain C_{max} (Eq. 6), precluding any excess density [25]. However, one common explosive, nitromethane, can produce dense plumes with SG = 1.06. We ran additional numerical simulations (Cases 7-9) to emulate nitromethane vapor plumes, with the results shown in Fig. 7. The resulting plumes are quite similar to the SG=1.29 cases shown in Fig. 5, despite the relatively large change in vapor density.

4 Laboratory Experiments

We conducted laboratory experiments to confirm the general findings of the numerical simulations from the previous section. We placed the TADD in a low-speed wind tunnel and used a photoionization detector (PID) to measure scalar concentrations in the downstream wake region (Fig. 8). The wind tunnel

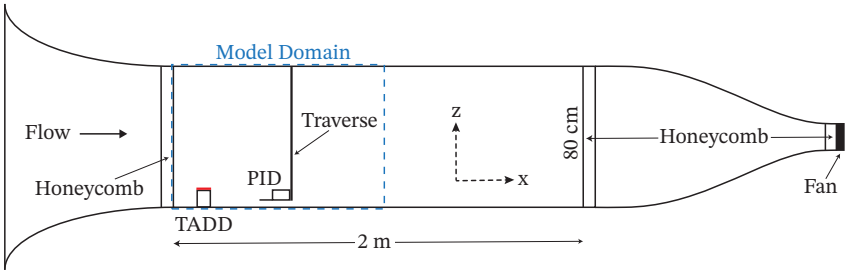

Fig. 8: Schematic of experimental configuration in 2 m x 0.8 m x 0.8 m low-speed wind tunnel. A computer-controlled traverse translates a photoionization detector transversely and vertically in the wake of the TADD. Honeycomb panels condition the crossflow and reduce the propagation of swirl from the fan. The dotted blue line denotes the corresponding numerical model domain.

has the same cross-sectional dimensions as the computational domain for the corresponding numerical simulations (dashed blue lines in Fig. 10).

A computer-controlled fan downstream of the test section draws ambient turbulent laboratory air through a bell-shaped contraction at the inlet and then into the 2 m x 0.8 m x 0.8 m test section. Upstream and downstream honeycomb panels help to isolate the flow in the test section from ambient flow variations and fan swirl. Flow speeds in the test section are measured using an anemometer (Kanomax Climomaster 6501 hot-wire). The fan speed is set such that the mean flow speed at the top of the TADD (measured without the TADD present) is 5.5 cm/s.

For the experiments, we use saturated acetone vapor (SG=1.29) as a surrogate odor for the hazardous materials (e.g., explosives or narcotics) typically associated with detection canine training. Acetone is advantageous in that it is relatively safe and inexpensive to use in the laboratory, has a molecular diffusivity ($1.05 \cdot 10^{-5}$ m^2/s) similar to many common explosives, and produces a strong response in PID instrumentation. To produce the acetone vapor, we partially filled the jar with liquid acetone, creating a saturated vapor headspace between the liquid surface and the vapor-permeable membrane at the top of the cylinder (Fig. 1).

We used the Aurora Scientific 200B miniPID to quantify the acetone vapor concentrations downstream of the cylinder. This PID has been used widely in academic and defense-related studies of scalar transport [30]. To calibrate the PID, we used mass flow controllers to combine five different ratios of saturated acetone vapor and pure air; these mixtures were delivered through a tube to the PID nozzle to generate calibration response curves. The experimental data was normalized by the saturated acetone vapor concentration C_{max} from Eq. 6 in units of ppm to compare to the numerical results.

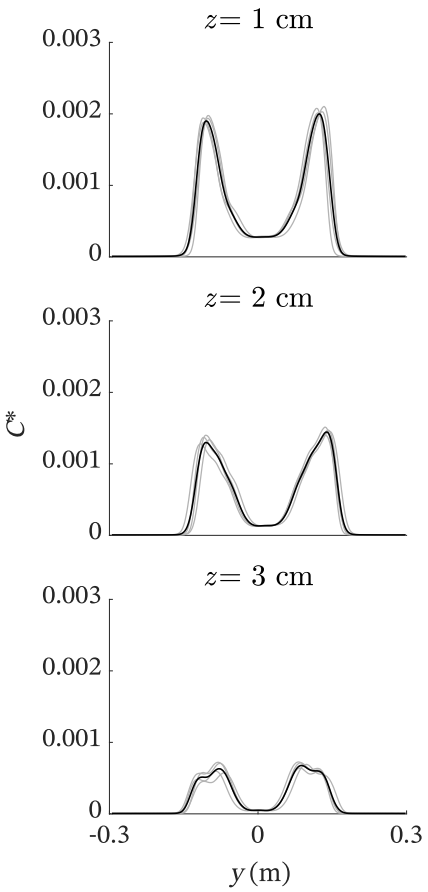

Fig. 9: Repeatability tests for lateral profiles of normalized odor concentration at x=40 cm in the laboratory experiments for U = 5.5 cm/s and SG=1.29. Four individual replicates (gray lines) are acquired for each location, which are then used to compute the ensemble average (black lines). Results are shown for three different vertical distances from the bed.

An automated traverse system was used to translate the PID laterally from y = -0.3 m to y = 0.3 m across the cylinder wake at a constant traverse speed of 2 cm/s while PID data were acquired continuously at 10 Hz (corresponding to 0.2 mm lateral resolution). Lateral concentration profiles were measured at x = 0.4 m and x = 0.7 m, and at 1 cm increments above the bed. Four replicates were acquired for each lateral profile. The experiments demonstrate excellent repeatability (Fig. 9) with minimal variations observed across experimental replicates. Each of four experimental replicates is shown in gray lines, and the black line denotes the ensemble average. The measured concentration profiles exhibit a high degree of lateral symmetry, and are insensitive to the

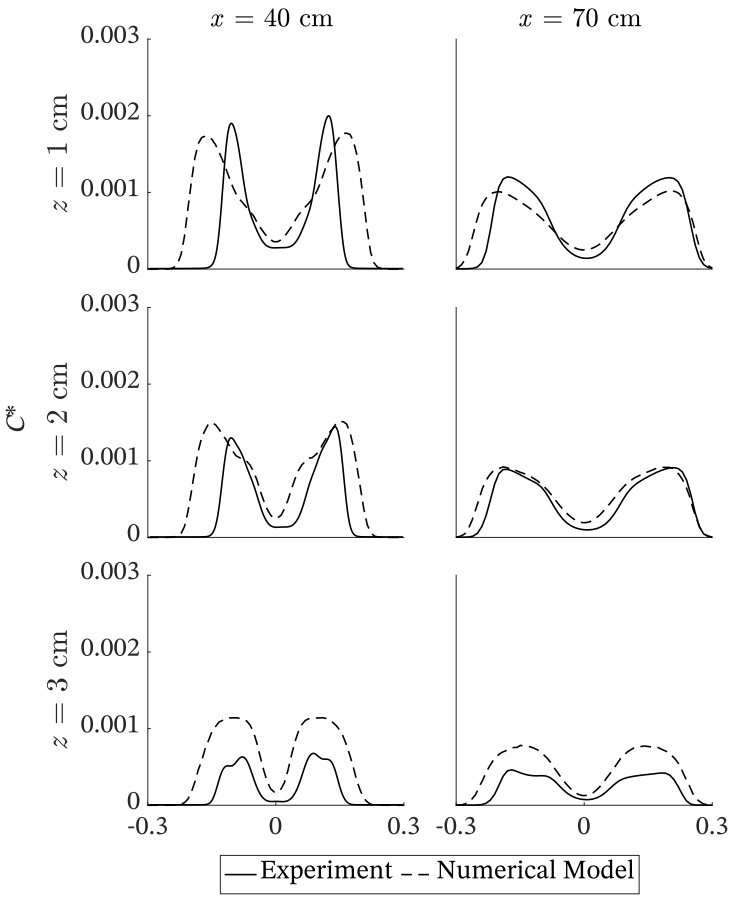

Fig. 10: Lateral profiles of normalized concentration for the laboratory experiments (solid lines) for $U = 5.5$ cm/s and SG = 1.29. Profiles are shown for two streamwise locations ($x = 40$ and 70 cm) and three vertical locations ($z =$ 1, 2 and 3 cm). Results from the corresponding numerical simulations (Case 5 from Table 1) are shown for comparison with dashed lines.

PID traverse direction. These results confirm the lack of any unsteady vortex shedding in the wake of the low-AR cylinder, consistent with the numerical simulations.

Ensemble-averaged lateral concentration profiles from the laboratory experiments are shown for two streamwise and three vertical locations as solid lines in (Fig. 10). For comparison, corresponding numerical simulations (Case 5 from Table 1) for each location are shown with dashed lines. The experiments capture the main structural features of the numerically simulated plumes, including the strong bimodality, lateral profile shape, lateral peak spreading with streamwise distance, and approximate concentrations. However, the scalar

magnitudes differ in some instances. These differences are likely associated with the lack of direct correspondence between the numerical and laboratory conditions. For computational efficiency, the numerical model domain included only the first half of the wind tunnel test section, and did not incorporate the bell-shaped contraction section (which modifies the inlet flow profile and boundary layer dynamics). The plume development is also highly sensitive to variations in SG (which, in turn depends on concentration and the degree of acetone vapor saturation).

5 Conclusion

The spatial distribution of a scalar plume in the wake of a finite-height cylinder in laminar crossflow is complex, driven primarily by inertial (Re) and density (Ri) effects. The plume characteristics presented here represent idealized conditions surrounding a common canine training device, with scalar contours well within the detection range of canine olfaction [2]. Experimental evaluation in a low-speed wind tunnel shows qualitative agreement with a numerical model of the test section, and the model is used to examine the dominant flow field features and to elucidate the impact of both velocity and density changes. Altering velocity modulates the width of the plume, decreasing the spread with increasing velocity. Increasing the density of the odor increases the width of the plume and results in a bimodal distribution due to interaction with and reinforcement of the horseshoe vortex. This study advances understanding of dense plume dispersal patterns in the wake of finite-height cylinders in laminar crossflow.

6 Acknowledgements

We thank Drs. Michele Maughan and Jenna Gadberry for their efforts to help conceptualize this project. Funding was received from DEVCOM-CBC for this project.

7 Declaration

The authors declare that they have no known competing financial interests or personal relationships that have influenced the work reported in this paper.

References

[1] Lai, H., Leung, A., Magee, M., Almirall, J.: Identification of volatile chemical signatures from plastic explosives by spme-gc/ms and detection by ion mobility spectrometry. Analytical and bioanalytical chemistry **396**, 2997–3007 (2010)

[2] Macias, M., Guerra-Diaz, P., Almirall, J., Furton, K.: Detection of piperonal emitted from polymer controlled odor mimic permeation systems utilizing canis familiaris and solid phase microextraction-ion mobility spectrometry. Forensic science international **195**(1–3), 132–8 (2010)

[3] Furton, K.G., Myers, L.J.: The scientific foundation and efficacy of the use of canines as chemical detectors for explosives. Talanta **54**(3), 487–500 (2001)

[4] Rezende, G.C., Le Calvé, S., Brandner, J.J., Newport, D.: Micro photoionization detectors. Sensors and Actuators B: Chemical **287**, 86–94 (2019)

[5] Wilson, A., Baietto, M.: Applications and advances in electronic-nose technologies. Sensors **9**(7), 5099–148 (2009)

[6] Karakaya, D., Ulucan, O., Turkan, M.: Electronic nose and its applications: A survey. International journal of Automation and Computing **17**(2), 179–209 (2020)

[7] Orix, D., Schmuker, M.: Resolving fast gas transients with metal oxide sensors. ACS Sensors **6**(3), 688–92 (2021)

[8] Joshi, M., Delgado, Y., Guerra, P., Lai, H., Almirall, J.: Detection of odor signatures of smokeless powders using solid phase microextraction coupled to an ion mobility spectrometer. Forensic Science International **188**(1–33), 112–8 (2009)

[9] Lazarowski, L., Waggoner, L.P., Krichbaum, S., Singletary, M., Haney, P.S., Rogers, B., Angle, C.: Selecting dogs for explosives detection: behavioral characteristics. Frontiers in Veterinary Science, 597 (2020)

[10] SciK9: Training Aid Delivery Device (TM) (2023). https://www.scik9.com/ Accessed 2023-11-21

[11] Essler, J.L., Kane, S.A., Nolan, P., Akaho, E.H., Berna, A.Z., DeAngelo, A., Berk, R.A., Kaynaroglu, P., Plymouth, V.L., Frank, I.D., *et al.*: Discrimination of sars-cov-2 infected patient samples by detection dogs: a proof of concept study. PLoS One **16**(4), 0250158 (2021)

[12] Sumner, D.: Flow above the free end of a surface-mounted finite-height circular cylinder: a review. Journal of Fluids and Structures **43**, 41–63 (2013)

[13] Okamoto, S., Sunabashiri, Y.: Vortex shedding from a circular cylinder of finite length placed on a ground plane (1992)

[14] Kumar, B., Mittal, S.: Prediction of the critical reynolds number for flow past a circular cylinder. Computer methods in applied mechanics and engineering **195**(44-47), 6046–6058 (2006)

[15] Nishioka, M., Sato, H.: Mechanism of determination of the shedding frequency of vortices behind a cylinder at low reynolds numbers. Journal of Fluid Mechanics **89**(1), 49–60 (1978)

[16] Okamoto, T., Yagita, M.: The experimental investigation on the flow past a circular cylinder of finite length placed normal to the plane surface in a uniform stream. Bulletin of JSME **16**(95), 805–814 (1973)

[17] Palau-Salvador, G., Stoesser, T., Fröhlich, J., Kappler, M., Rodi, W.: Large eddy simulations and experiments of flow around finite-height cylinders. Flow, turbulence and combustion **84**, 239–275 (2010)

[18] Baker, C.: The laminar horseshoe vortex. Journal of fluid mechanics **95**(2), 347–367 (1979)

[19] Fisher, E., Eibeck, P.: The influence of a horseshoe vortex on local convective heat transfer (1990)

[20] Lee, L.W.: Wake structure behind a circular cylinder with a free end. In: Proceedings of the Heat Transfer and Fluid Mechanics Institute, pp. 241–251 (1997). Stanford Univ. Press

[21] Palau-Salvador, G., García-Villalba, M., Rodi, W.: Scalar transport from point sources in the flow around a finite-height cylinder. Environmental fluid mechanics **11**, 611–625 (2011)

[22] Fay, J.: Buoyant plumes and wakes. Annual Review of Fluid Mechanics **5**(1), 151–160 (1973)

[23] Little, S.A., Stolzenbach, K.D., Von Herzen, R.P.: Measurements of plume flow from a hydrothermal vent field. Journal of Geophysical Research: Solid Earth **92**(B3), 2587–2596 (1987)

[24] Schatzmann, M., Snyder, W.H., Lawson Jr, R.E.: Experiments with heavy gas jets in laminar and turbulent cross-flows. Atmospheric Environment. Part A. General Topics **27**(7), 1105–1116 (1993)

[25] Ewing, R.G., Waltman, M.J., Atkinson, D.A., Grate, J.W., Hotchkiss, P.J.: The vapor pressures of explosives. TrAC Trends in Analytical Chemistry **42**, 35–48 (2013)

[26] Schenk, O., Gärtner, K., Fichtner, W., Stricker, A.: Pardiso: a high-performance serial and parallel sparse linear solver in semiconductor device simulation. Future Generation Computer Systems **18**(1), 69–78 (2001)

[27] Hunt, J.C., Wray, A.A., Moin, P.: Eddies, streams, and convergence zones in turbulent flows. Studying turbulence using numerical simulation databases, 2. Proceedings of the 1988 summer program (1988)

[28] Zhan, J.-m., Li, Y.-t., Wai, W.-h.O., Hu, W.-q.: Comparison between the q criterion and rortex in the application of an in-stream structure. Physics of Fluids **31**(12) (2019)

[29] Sumner, D., Heseltine, J., Dansereau, O.: Wake structure of a finite circular cylinder of small aspect ratio. Experiments in Fluids **37**, 720–730 (2004)

[30] True, A.C., Crimaldi, J.P.: Distortion of passive scalar structure during suction-based plume sampling. Sensors and Actuators B: Chemical **367**, 132018 (2022)